Unsupervised Discovery of Spatiotypes and Context-Aware Graph Neural Networks for Modeling Clinical Endpoints

Muhammad Dawood[1,2⋆], Emily Thomas[1,2], Rosalin Cooper[1,3], Carlo Pescia[4], Anna Sozanska[1], Hosuk Ryou[1,2], Daniel Royston[1,3], and Jens Rittscher[2]

[1]Nuffield Division of Clinical Laboratory Sciences, University of Oxford, Oxford, UK
[2]Institute of Biomedical Engineering, University of Oxford, Oxford, UK
[3]Oxford University Hospitals, Oxford, UK
[4]Division of Pathology, ASST Santi Paolo e Carlo, Milan, Italy
muhammad.dawood@ndcls.ox.ac.uk

Abstract. Human tissue samples exhibit remarkable cellular and structural diversity, where alterations in the spatial arrangement of cells can signal the onset or progression of disease. Therefore, characterizing these spatial cellular interactions and linking them to clinical endpoints is critical to advance our understanding of disease biology and improve patient care. In this work, we introduce a *band descriptor* that quantifies the local neighborhood of each cell by computing the relative abundance of neighboring cell types using concentric bands. We demonstrate the efficacy of our approach by highlighting two key benefits: it enables the unsupervised discovery of *spatiotypes* (substructures defined by local cellular configurations), and it provides an explicit encoding of spatial context in cell-level graphs — capturing long-range cell interactions across tissue. Our experiments in a lung tissue cohort reveal distinct spatial patterns of cellular arrangement that differentiate control from disease samples and may also reflect disease progression (unaffected, less affected, or more affected). Furthermore, by explicitly modeling spatial context, our band descriptor enhances node-level representations, enabling an end-to-end Graph Neural Network (GNN) to achieve high accuracy in a clinical prediction task with fewer layers. This reduction in network depth decreases over-smoothing and improves interpretability, underscoring our approach's potential for broad adoption in tissue-based studies and clinical applications. Code is available on GitHub[1].

Keywords: Band Descriptor · Spatiotypes · Graph Neural Network

1 Introduction

The spatial organization of cells within human tissues profoundly influences their phenotypes, states, and biological behavior by modulating the signals they re-

⋆ Corresponding author: muhammad.dawood@ndcls.ox.ac.uk
[1] https://github.com/imuhdawood/BandDescriptor

ceive [1, 3, 20]. Whole Slide Images (WSIs) provide snapshots of this organization, capturing rich morphological and spatial information in multi-gigapixel scans [13]. However, analyzing WSIs at full resolution is computationally demanding. To address this, WSIs are typically partitioned into smaller patches, from which statistical or morphological features are extracted and aggregated for downstream tasks such as predicting disease status [14], molecular characteristics [10, 17, 15], drug sensitivity [11], or patient survival [18].

Current aggregation approaches can be broadly classified as either spatially unaware or spatially aware [7]. Spatially unaware methods, often employing multiple instance learning (MIL), treat each WSI as a "bag" of patches and aggregate patch-level scores without modeling their spatial relationships. In contrast, spatially aware methods utilise a graph representation — where each node denotes a spatial region or patch — capturing a bespoke local context via node features [23, 9]. A GNN is then trained to capture information from close proximal nodes using message passing [17, 8]. While both strategies have shown promise in several predictive tasks [9, 7, 16, 11], they frequently overlook local cellular microenvironments — essential determinants of tissue function and disease outcomes [21].

Recent progress in image-based transcriptomics, which provides single-cell resolution of gene expression and cellular/nuclear boundaries, requires a spatially resolved analysis that can be linked to biological hypotheses or questions [3, 21, 19]. Although graph-based models can, in principle, incorporate these rich features, capturing long-range interactions within a tissue often demands deep architectures that risk oversmoothing and reduced interpretability [26]. Moreover, in addition to predicting clinical endpoints, these data warrant identifying spatial cellular microenvironmental patterns linked to disease.

To address these gaps, we propose a *band descriptor* that captures local cellular arrangements around each cell using concentric bands, preserving the microenvironmental context essential for understanding disease. Leveraging these descriptors, we discover spatiotypes in an unsupervised manner and enhance GNN-based prediction, integrating single-cell detail with tissue-scale analyses. In lung tissue samples, the spatiotypes uncovered by our approach effectively distinguish control and disease groups while also predicting disease state. Furthermore, incorporating the *band descriptor* into shallow GNNs boosts accuracy, mitigates oversmoothing, and improves interpretability of node-level prediction scores, underscoring its potential for clinical applications.

2 Dataset

To evaluate our approach, we used lung tissue data from a recent study that profiled 343 genes in 45 lung tissue samples, including 9 from unaffected donors and 26 from lung transplant recipients with pulmonary fibrosis, with some patients contributing multiple sections [21]. The study used the Xenium platform (10x Genomics), an image-based spatial transcriptomics technology that provides high-resolution spatial transcript data, cellular and nuclear boundaries,

while preserving tissue for post-run H&E staining. Based on marker gene expression, the authors classified cells into four key lineages: epithelial, endothelial, mesenchymal, and immune cells, which we used in this study. We restricted our analysis to coarse-grained as these could be also be inferred from morphology.

3 Methods

4 Band Descriptor

As illustrated in Figure 1, we begin with a WSI where each detected cell has a spatial location (centroid) and an assigned type. Building on existing work on shape and context descriptors [2, 4, 5] we construct a local neighborhood consisting of concentric circles of different radii that are centered on a cell of interest. In each radial band defined we quantify the spatial distribution of neighboring cell types, forming a multi-scale descriptor that encodes both immediate and distant neighborhood composition.

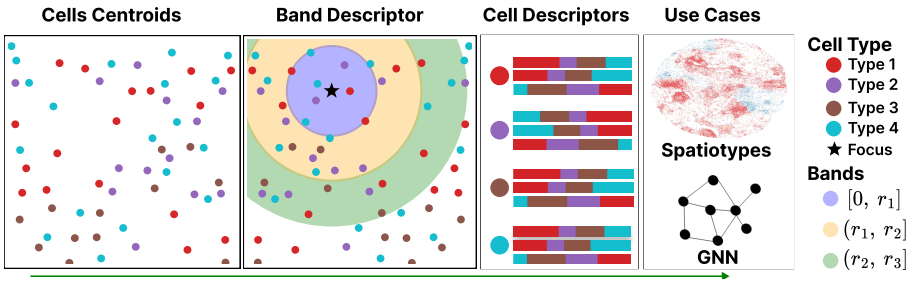

Fig. 1. Overview of our proposed band descriptor approach. **(Left)** Cell centroids, color-coded by type, within a tissue image. **(Second)** A focal cell (star) surrounded by concentric bands $[0, r_1)$, $[r_1, r_2)$, $[r_2, r_3)$, capturing multi-scale neighborhood composition. **(Third)** Computed band descriptors for each cell type, quantifying the fraction of neighboring cell types within each band. **(Right)** Example applications include spatiotype discovery (via clustering) and clinical endpoint prediction using a graph neural network (GNN).

To formalize this approach, we consider a dataset $D = \{(x_i, y_i, t_i, s_i) \mid i = 1, \ldots, N\}$, where each cell has a location (x_i, y_i), type $t_i \in T$, and an associated tissue section or slide ($s_i \in S$). To capture the microenvironment of a given cell i, we define a strictly increasing sequence of radii $\{r_k\}_{k=1}^{K+1}$, where $r_1 = 0$. Each concentric band (or ring) $k \in \{1, \ldots, K\}$ then corresponds to the distance interval $[r_k, r_{k+1})$. Specifically, the k-th ring around the cell i is:

$$\beta_i^k = \{j \neq i : s_j = s_i,\ r_k \leq d((x_i, y_i), (x_j, y_j)) < r_{k+1}\}\,.$$

where $d(\cdot,\cdot)$ is a spatial distance metic. For a given cell type $T^* \in T$, we define the subset $D^{(T^*)} = \{i \mid t_i = T^*\}$. For each cell in $i \in D^{(T^*)}$, we quantify the composition of different cell types $t \in T$ in ring k as:

$$f_{i,t}^k = \frac{1}{|\beta_i^k|} \sum_{j \in \beta_i^k} \mathbb{1}\{t_j = t\},$$

In the above equation $|\beta_i^k|$ is the number of neighbors in ring k, and $\mathbb{1}\{\cdot\}$ is the indicator function. We then concatenate these band-level cell fractions across all rings $k = 1, \ldots, K$ to obtain a comprehensive microenvironment descriptor of cell i:

$$\mathbf{h}_i = \big(f_{i,1}^1, \ldots, f_{i,|T|}^1, f_{i,1}^2, \ldots, f_{i,|T|}^2, \ldots, f_{i,1}^K, \ldots, f_{i,|T|}^K\big),$$

The vector $\mathbf{h}_i \in \mathbb{R}^{|T| \times K}$ captures the multi-scale spatial composition of a cell's neighborhood, forming the basis for subsequent analyses of *spatiotypes* discovery or incorporating spatial context into a GNN.

5 Unsupervised Discovery of Spatiotypes

Cells of the same type can exhibit different spatial arrangements, reflecting different local environments. To uncover these spatial cellular patterns (*spatiotypes*), we cluster the band descriptors $\mathbf{h}_i$ of cells of a given type T^* into C groups using a Gaussian Mixture Model (GMM), assigning each cell i a refined microenvironmental subtype label $\hat{t}_i = T^*_{(c_i)}$. This label encodes the spatial relationship of a cell with surrounding cell types. For example, among immune cells (t_i = "Immune"), type 1 may correspond to immune cells predominantly surrounded by other immune cells, while type 2 may capture those adjacent to stromal cells, reflecting different spatiotypes. Repeating this for each T^* refines broad cell-type categories into interpretable subtypes that capture tissue-specific patterns.

The proposed approach is inherently explainable: the band-level descriptor $\mathbf{h}_i$ for each cell provides summary statistics detailing the composition of its microenvironment. Visualizing these statistics for each GMM-derived spatiotype provides insights into the underlying spatial patterns and tissue organization. These spatiotypes could also be used as node-level features in a GNN.

5.1 Modeling Context in a GNN for Clinical Endpoint Prediction

To assess the predictive utility of the proposed band descriptor $\mathbf{h}_i$, we represent the WSI of each tissue sample as a cell-level graph $G = (V, E)$. Here, each node $v_i \in V$ corresponds to a detected cell, and edges in E capture spatial adjacency based on Delaunay triangulation — connecting any two cells v_i and v_j that share a simplex and satisfy $d(v_i, v_j) \leq 50\,\mu m$. Building on the *SlideGraph*$^\infty$ framework [10], we employ a stack of EdgeConv layers [24] to learn aggregated node embeddings over an l-hop neighborhood in an end-to-end manner using pairwise ranking loss. We hypothesize that incorporating $\mathbf{h}_i$ directly as a node

representation captures both fine-grained (proximal bands) and long-range (distal bands) spatial interactions, thereby facilitating a direct link between cellular organization and clinical endpoints. Additionally, it enhances interpretability by leveraging a simple linear model to explain node-level predictions from *SlideGraph*$^{\infty}$, thereby revealing key spatial cellular arrangements that drive predictive signals.

6 Experiments and Results

6.1 Unsupervised Discovery of Clinically Relevant Spatiotypes

Experimental Design We computed the band descriptors for each major cell (endothelial, mesenchymal, epithelial, and immune) using five concentric bands with radii of $[100, 200, 300, 400, 500]\,\mu m$. The resulting cell-level descriptors were then clustered using a Gaussian Mixture Model (GMM), yielding 3 endothelial, 5 mesenchymal, 2 epithelial, and 6 immune spatiotypes. Each spatiotype captures a distinct pattern of spatial cellular composition (Figure 2A).

Quantitative Results At the patient-level, proportions of these spatiotypes differed significantly between control and disease groups and provides insights into disease trajectory (see Figure 2B). For instance, Endothelial-1 (endothelial cells surrounded by immune cells and loosely packed mesenchymal cells) shows a decreasing pattern of enrichment from unaffected to more fibrotic tissue (FDR-corrected p-value < 0.05 from a two-sided Wilcoxon test), suggesting that immune cell interactions contribute to vascular homeostasis. As this protective environment declines, endothelial dysfunction may set in, potentially driving vascular changes that promote fibrosis [6, 12]. Additionally, certain spatiotypes were exclusive to either disease or control groups. For example, *Immune-2* (immune cells densely clustered with other immune cells) are present only in fibrotic cases. Our findings align with a recent study reporting an increased proportion of immune cells in pulmonary fibrosis [25]. These results suggest that, despite being identified through a data-driven approach, spatiotypes can provide meaningful insights into the spatial cellular landscape and its connection to disease status and progression.

Visual Results To validate these findings spatially, we present example plots comparing a more fibrotic and a normal case (Figure 2C). Consistent with the boxplot results, the fibrotic sample shows a higher proportion of *Immune-2* (shown in blue), while in the normal case, most immune cells are in an *Immune-1* microenvironment. Similarly, in the fibrosis, endothelial cells exhibits both *Endothelial-1* and *Endothelial-2* spatiotype, whereas the normal case is enriched only for *Endothelial-1*, which based on the boxplot analysis is associated with normal tissue.

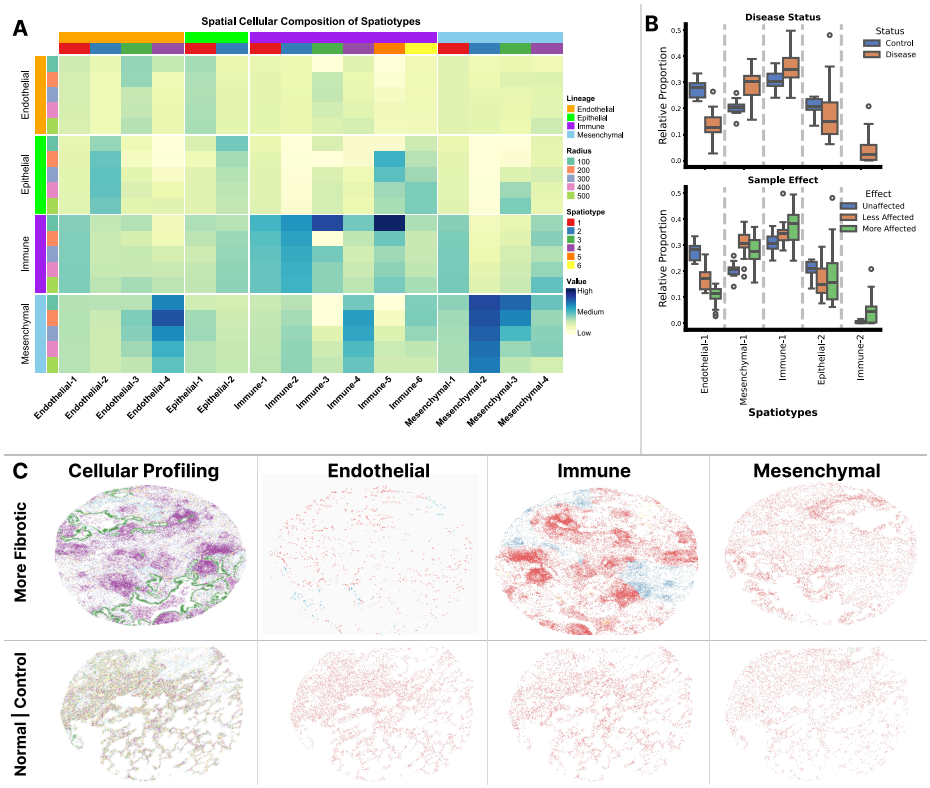

Fig. 2. Unsupervised Discovery of Clinically Relevant Spatiotypes. **(A)** Heatmap of distinct spatiotypes (columns), each capturing a unique spatial pattern of cellular composition, identified through unsupervised analysis. Rows correspond to spatial radii (100–500 μm), illustrating how cell composition varies across spatial scales. Spatiotypes are grouped by major cell lineages: endothelial, epithelial, immune, and mesenchymal. **(B)** Boxplots depicting the enrichment of spatiotypes across samples, stratified by disease status (Control vs. Disease) and disease state (Unaffected, Less Affected, More Affected). **(C)** Spatial maps comparing fibrotic (top) and control (bottom) lung tissue. The first column visualizes cell centroids colored by cell type (using the same colormap as in heatmap **(A)**). The remaining columns highlight spatiotype enrichment for each cell lineage, demonstrating differential spatial patterns between control and fibrotic samples.

7 Clinical Endpoint Prediction Using Graph Neural Networks

7.1 Experimental Setup

We demonstrate how the proposed band descriptor can be used to incorporate spatial context into a GNN for classifying unaffected versus more affected lung tissue. Below, we detail the experiments conducted to illustrate how different

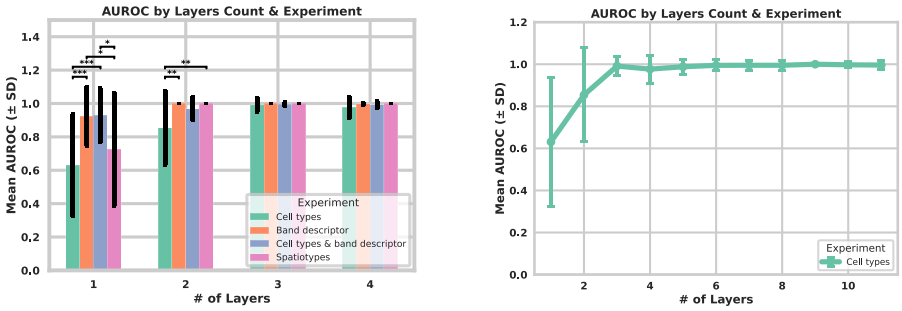

Fig. 3. (Left) AUROC for different node-level features across GNN layers. (Right) AUROC for cell-type-only GNN across increasing layers. Statistically significant results from a two-sided wilcoxon rank-sum test, corrected for false discovery, are indicated with asterisks: $*p < 0.05$, $**p < 0.01$, and $***p < 0.001$ in the (Left) plot.

node-level embeddings in a cell graph influence both predictive performance and model interpretability which are divided into the four different groups:

1. **Cell types**: One-hot encoding of cell types (endothelial, mesenchymal, epithelial, immune).
2. **Band descriptors**: Cell level band-descriptor without explicit cell-type encoding.
3. **Cell types + band descriptors**: Cell types combined with band descriptors.
4. **Spatiotypes**: Each node labeled by its spatiotype (discovered in Section 7).

7.2 Results

We assess the impact of different node-level embeddings using patient-level stratified bootstrapping (67% training, 33% testing, 20 repetitions). For each test set, we report the area under the receiver operating characteristic curve (AUROC) as the performance metric.

As shown in Figure 3, the band descriptors with a single-layer GNN achieves an AUROC of 0.92 ± 0.18, significantly outperforming cell types alone (0.63 ± 0.31). The spatiotypes yields a higher AUROC (0.73 ± 0.34) compared to cell types but remains notably lower than the band descriptors. Additionally, combining both cell types and the band descriptors provides a slight improvement (0.93 ± 0.16) in predictive performance compared to either feature alone. At two layers, the band descriptors, cell types + band descriptors, and spatiotypes all achieve an AUROC of 1.00, whereas cell types alone improve to 0.85 ± 0.22. Notably, cell types require a deep, nine-layer GNN to reach an AUROC of 1.00 (see Figure 3), whereas the same GNN, when leveraging the band descriptor, achieves the same accuracy with only two layers — reducing the risk of over-smoothing and improving the interpretability of node-level scores [26].

Node-level Features	(α, λ)	$\mathbf{R^2}$	MSE	MAE
Environ	(0.001, 0.10)	0.451 (0.075)	0.021 (0.002)	0.123 (0.005)
Band Descriptor	(0.001, 0.10)	0.921 (0.038)	0.001 (0.001)	0.023 (0.007)
Cell Type	(0.001, 0.10)	0.226 (0.062)	0.020 (0.002)	0.119 (0.006)

Table 1. Node-level score prediction using different feature descriptors. Here, α and λ are the L1 and L2 regularization penalties, respectively, and the rest of columns reports mean (standard deviation) of model across 5 cross-validation runs in terms of R^2, mean squared error (MSE) and mean absolute error (MAE).

7.3 Interpretability

We analyzed the interpretability of node-level scores using three types of node embeddings: cell types, band descriptors, and spatiotypes. To assess this, we fit an Elastic-Net regression model to predict node importance scores from node-level features. After optimizing regularization parameters, we evaluated model performance using mean squared error (MSE), mean absolute error (MAE), and R^2 score, as shown in Table 1. From the results, using the band descriptors with a 2-layer GNN enabled highly accurate node-level predictions, achieving a significantly higher R^2 score compared to using cell type information with a 9-layer GNN. This demonstrates that the band descriptor not only improves accuracy but also enhances interpretability — critical for clinical applications. Additionally, visualizing feature contributions allows us to identify key spatial bands around a cell that drive predictions.

8 Discussion & Conclusion

Our results highlight two key contributions of the proposed band descriptor. First, by encoding the spatial composition of different cell types around each cell using concentric bands, it enables the discovery of *spatiotypes* that differentiate disease samples from controls in an interpretable and clinically meaningful way. Second, by explicitly modeling multi-scale spatial context within a GNN through enriched cell-level representations, our descriptor achieves high predictive performance even with a shallow architecture, reducing the need for deeper networks that often risk over-smoothing. Unlike most methods that achieve explainability post-hoc, our approach inherently integrates spatial context into the model, enabling direct and clinically meaningful interpretability without requiring additional explanation techniques — striking a crucial balance between accuracy and interpretability in clinical applications [27, 22].

Beyond lung fibrosis, analogous to shape context features used for detection and information retrieval, the proposed band descriptor supports broader applications across diverse tissue types and spatial omics platforms, including multi-

plex fluorescence imaging and high-dimensional spatial transcriptomics. It seamlessly extends to 3D imaging modalities, addressing the challenge of capturing spatial structures in volumetric data. It can be adapted for the targeted analysis of spatial transcriptomic patterns, ultimately bridging single-cell or transcriptomic resolution with tissue-scale analyses.

Acknowledgements

This work was supported by Blood Cancer UK and Cancer Research UK.

Disclosure of Interests

Rittscher is a current equity holder in Ground Truth Labs Ltd. Royston reports consultancy with Ground Truth Labs Ltd. and Johnson & Johnson.

References

1. Adegunsoye, A., Kropski, J.A., Behr, J., Blackwell, T.S., Corte, T.J., Cottin, V., Glanville, A.R., Glassberg, M.K., Griese, M., Hunninghake, G.M., et al.: Genetics and genomics of pulmonary fibrosis: charting the molecular landscape and shaping precision medicine. American Journal of Respiratory and Critical Care Medicine **210**(4), 401–423 (2024)
2. Asif, A., Dawood, M., Jan, B., Khurshid, J., DeMaria, M., Minhas, F.u.A.A.: Phurie: hurricane intensity estimation from infrared satellite imagery using machine learning. Neural Computing and Applications **32**, 4821–4834 (2020)
3. Bandyopadhyay, S., Duffy, M.P., Ahn, K.J., Sussman, J.H., Pang, M., Smith, D., Duncan, G., Zhang, I., Huang, J., Lin, Y., et al.: Mapping the cellular biogeography of human bone marrow niches using single-cell transcriptomics and proteomic imaging. Cell **187**(12), 3120–3140 (2024)
4. Belongie, S., Malik, J., Puzicha, J.: Shape context: A new descriptor for shape matching and object recognition. Advances in neural information processing systems **13** (2000)
5. Belongie, S., Malik, J., Puzicha, J.: Shape matching and object recognition using shape contexts. IEEE transactions on pattern analysis and machine intelligence **24**(4), 509–522 (2002)
6. Bian, F., Lan, Y.W., Zhao, S., Deng, Z., Shukla, S., Acharya, A., Donovan, J., Le, T., Milewski, D., Bacchetta, M., et al.: Lung endothelial cells regulate pulmonary fibrosis through foxf1/r-ras signaling. Nature Communications **14**(1), 2560 (2023)
7. Bilal, M., Jewsbury, R., Wang, R., AlGhamdi, H.M., Asif, A., Eastwood, M., Rajpoot, N.: An aggregation of aggregation methods in computational pathology. Medical Image Analysis **88**, 102885 (2023)
8. Brussee, S., Buzzanca, G., Schrader, A.M., Kers, J.: Graph neural networks in histopathology: Emerging trends and future directions. Medical Image Analysis p. 103444 (2025)
9. Chen, R.J., Ding, T., Lu, M.Y., Williamson, D.F., Jaume, G., Song, A.H., Chen, B., Zhang, A., Shao, D., Shaban, M., et al.: Towards a general-purpose foundation model for computational pathology. Nature Medicine **30**(3), 850–862 (2024)

10. Dawood, M., Eastwood, M., Jahanifar, M., Young, L., Ben-Hur, A., Branson, K., Jones, L., Rajpoot, N., et al.: Cross-linking breast tumor transcriptomic states and tissue histology. Cell Reports Medicine **4**(12) (2023)
11. Dawood, M., Vu, Q.D., Young, L.S., Branson, K., Jones, L., Rajpoot, N., Minhas, F.u.A.A.: Cancer drug sensitivity prediction from routine histology images. NPJ Precision Oncology **8**(1), 5 (2024)
12. Fließer, E., Jandl, K., Lins, T., Birnhuber, A., Valzano, F., Kolb, D., Foris, V., Heinemann, A., Olschewski, H., Evermann, M., et al.: Lung fibrosis is linked to increased endothelial cell activation and dysfunctional vascular barrier integrity. American Journal of Respiratory Cell and Molecular Biology **71**(3), 318–331 (2024)
13. Ghaznavi, F., Evans, A., Madabhushi, A., Feldman, M.: Digital imaging in pathology: whole-slide imaging and beyond. Annual Review of Pathology: Mechanisms of Disease **8**(1), 331–359 (2013)
14. Graham, S., Minhas, F., Bilal, M., Ali, M., Tsang, Y.W., Eastwood, M., Wahab, N., Jahanifar, M., Hero, E., Dodd, K., et al.: Screening of normal endoscopic large bowel biopsies with interpretable graph learning: a retrospective study. Gut **72**(9), 1709–1721 (2023)
15. Kather, J.N., Heij, L.R., Grabsch, H.I., Loeffler, C., Echle, A., Muti, H.S., Krause, J., Niehues, J.M., Sommer, K.A., Bankhead, P., et al.: Pan-cancer image-based detection of clinically actionable genetic alterations. Nature cancer **1**(8), 789–799 (2020)
16. Kather, J.N., Pearson, A.T., Halama, N., Jäger, D., Krause, J., Loosen, S.H., Marx, A., Boor, P., Tacke, F., Neumann, U.P., et al.: Deep learning can predict microsatellite instability directly from histology in gastrointestinal cancer. Nature medicine **25**(7), 1054–1056 (2019)
17. Lu, W., Toss, M., Dawood, M., Rakha, E., Rajpoot, N., Minhas, F.: Slidegraph+: Whole slide image level graphs to predict her2 status in breast cancer. Medical Image Analysis **80**, 102486 (2022)
18. Mackenzie, C.C., Dawood, M., Graham, S., Eastwood, M., et al.: Neural graph modelling of whole slide images for survival ranking. In: Learning on Graphs Conference. pp. 48–1. PMLR (2022)
19. Moffitt, J.R., Bambah-Mukku, D., Eichhorn, S.W., Vaughn, E., Shekhar, K., Perez, J.D., Rubinstein, N.D., Hao, J., Regev, A., Dulac, C., et al.: Molecular, spatial, and functional single-cell profiling of the hypothalamic preoptic region. Science **362**(6416), eaau5324 (2018)
20. Su, J., Song, Y., Zhu, Z., Huang, X., Fan, J., Qiao, J., Mao, F.: Cell–cell communication: new insights and clinical implications. Signal Transduction and Targeted Therapy **9**(1), 196 (2024)
21. Vannan, A., Lyu, R., Williams, A.L., Negretti, N.M., Mee, E.D., Hirsh, J., Hirsh, S., Hadad, N., Nichols, D.S., Calvi, C.L., et al.: Spatial transcriptomics identifies molecular niche dysregulation associated with distal lung remodeling in pulmonary fibrosis. Nature Genetics pp. 1–12 (2025)
22. di Villaforesta, A.F., Magister, L.C., Barbiero, P., Liò, P.: Digital histopathology with graph neural networks: Concepts and explanations for clinicians. arXiv preprint arXiv:2312.02225 (2023)
23. Wang, X., Yang, S., Zhang, J., Wang, M., Zhang, J., Yang, W., Huang, J., Han, X.: Transformer-based unsupervised contrastive learning for histopathological image classification. Medical image analysis **81**, 102559 (2022)
24. Wang, Y., Sun, Y., Liu, Z., Sarma, S.E., Bronstein, M.M., Solomon, J.M.: Dynamic graph cnn for learning on point clouds. ACM Transactions on Graphics (tog) **38**(5), 1–12 (2019)

25. Wei, X., Jin, C., Li, D., Wang, Y., Zheng, S., Feng, Q., Kong, W., Ma, X., Wang, J., et al.: Single-cell transcriptomics reveals cd8+ t cell structure and developmental trajectories in idiopathic pulmonary fibrosis. Molecular Immunology **172**, 85–95 (2024)
26. Wu, X., Chen, Z., Wang, W., Jadbabaie, A.: A non-asymptotic analysis of over-smoothing in graph neural networks. arXiv preprint arXiv:2212.10701 (2022)
27. Ying, Z., Bourgeois, D., You, J., Zitnik, M., Leskovec, J.: Gnnexplainer: Generating explanations for graph neural networks. Advances in neural information processing systems **32** (2019)